Kirigami Metasurfaces for Bioinspired Assistive Shoe Grips

Sahab Babaee[1,2]†, Simo Pajovic[1,2]†, Ahmad Rafsanjani[3]†, Yichao Shi[2,4], Katia Bertoldi[5]*, Giovanni Traverso[1,6]*

[1]Department of Mechanical Engineering, Massachusetts Institute of Technology, Cambridge, MA 02139, USA

[2]Department of Chemical Engineering and Koch Institute for Integrative Cancer Research, Massachusetts Institute of Technology, Cambridge, MA 02139, USA

[3]Department of Materials, ETH Zurich, 8093 Zürich, Switzerland

[4]University of Toronto, Toronto, Ontario, Canada

[5]John A. Paulson School of Engineering and Applied Sciences, Harvard University, Cambridge, MA 02138, USA

[6]Division of Gastroenterology, Department of Medicine, Brigham and Women's Hospital, Harvard Medical School, Boston, MA 02115, USA

†These authors contributed equally to this work.

*Corresponding authors. E-mail: bertoldi@seas.harvard.edu (K.B.); cgt20@mit.edu (G.T.)

Abstract: Falls and subsequent complications are major contributors to morbidity and mortality, especially in older adults. To address this problem, we aimed to develop a lightweight, dynamic device to increase friction between the shoe and the walking surface that is effective across a range of surfaces, particularly ice. Inspired by claws and scales found in nature, we developed a range of kirigami structures that could be applied to footwear outsoles to generate higher friction forces in the forefoot. We evaluated those metasurfaces through numerical simulations, in vitro surface interaction, and in vivo human force plate measurement to identify optimal kirigami designs capable of modulating friction across a range of surfaces. We anticipate the potential application of these systems could help mitigate the risk of falls in a range of environments.

Falls are a common health problem with a tremendous impact on morbidity and mortality. Falls are ranked as the first leading cause of death for older adults[1] and the second leading cause of occupational-related deaths[2]. Musculoskeletal injuries associated with falls include hip fractures, which dramatically increase morbidity and mortality in older adults: nearly half of the patients with hip fractures are unable to return to living independently[3], and mortality rates twelve months after hip fracture are 12-37%[4-7]. Moreover, the direct costs of fatal and non-fatal falls are estimated to be greater than $64 billion per year in the United States[8-10]. Considering the dangers and costs associated with fall injuries, particularly for high frequency work injuries involving ice[11], there have been efforts to understand and prevent slips and falls[12–16], including evaluation of the impact of footwear technologies and the ways in which their basic properties (e.g., sole hardness) affect slip resistance[15–20]. Existing devices such as crampons and snow chains attach to the soles of shoes to increase grip, but protrude from the sole at all times and may be tedious to attach and detach. Thus, there is a need for lightweight, dynamic devices that can help prevent slips and falls through friction enhancement of footwear.

Kirigami – the Japanese art of paper cutting – has become a powerful tool for developing highly flexible devices and transformable structures[21–24]. Kirigami surfaces are capable of buckling-induced shape transformation from flat sheets to 3D textured surfaces and have been employed in a broad range of applications including light manipulation[25], energy harvesting[26], wearable thermotherapy[27], crawling locomotion[28], flexible sensors and actuators[29,30], stretchable bioprobes[31], conductive nanocomposites[32,33], and lithium-ion batteries[34]. Recently, the anisotropic friction of a kirigami skin enabled locomotion of a crawling soft robot[28]. Here, inspired by active friction control strategies in animals using claws and scales, yet recognizing the differences in their niches to where our systems would be applied, we report a kirigami-based assistive shoe grip to reduce the risks of slips and falls. We demonstrate the ability to dynamically modulate friction using highly stretchable lightweight kirigami patches comprising of steel sheets perforated with a periodic array of scale-like spikes. When stretched, the spikes buckle out, resulting in engagement with the surface in contact and a higher friction force. Through a combination of simulations and experiments, we carefully chose the perforation template such that the resulting spikes are stiff and buckle out at the largest possible angle of attack to maximize engagement of the kirigami grip with the contacting surface. These kirigami patches could serve as a new class of slip-resistant footwear add-ons, which can be tuned to enhance friction between the shoe and specific walking and working surfaces, thereby reducing the risk of slips and falls across many potentially hazardous environments.

Nature is a rich source of inspiration for friction-enhancement designs. **Fig. 1A** shows examples of animals in nature that exploit dynamic modulation of friction for locomotion and gripping. These animals utilize anatomical structures and mechanisms to selectively and transiently increase friction on certain surfaces or in certain situations. For example, cheetahs have semi-retractable claws that increase friction when turning while chasing prey and climbing[35].

Oxpeckers' sharp claws point in opposing directions to provide a strong grip and stable positioning while riding on the backs of larger mammals ranging from cattle to rhinoceroses[36]. Snakes orient their scales to increase friction anisotropy and propel themselves forward in rectilinear[37] and serpentine locomotion[38]. Inspired by these animals, we developed slip-resistant assistive kirigami grips that can be attached to the soles of the shoes. **Fig. 1B** shows the undeformed and deformed configurations of a steel kirigami shoe grip with concave spikes attached to the shoe soles. During walking, the bending of the shoe soles induces stretching in the patches and causes the spikes to buckle outward from the soles (Movie S1). Engagement of spikes with the walking surface results in a considerable change in the tribological behaviour of the shoes. The kirigami surfaces were engineered to undergo a reversible shape transformation from flat surfaces (corresponding to low friction) to 3D textured surfaces with popped-up spikes (corresponding to high friction). Kirigami patches allow similarly dynamic friction modulation by remaining flat when the wearer is standing still and transforming increase friction specifically during walking. The patches thereby improve resistance to slips and falls without the hassle or possible discomfort of obtrusive attachments.

Fig 1. Kirigami shoe grip for dynamic modulation of friction and preventing slips and falls. (**A**) Inspiration from friction-enhancing strategies in animals: cheetah with semi-retractable claws[35], oxpecker with sharp claws in opposing directions[36], and snake with scales which are oriented to increase friction[37]. (**B**) Kirigami for friction modulation in footwear. Steel kirigami surfaces were attached to the shoe soles.

The undeformed and deformed configurations of the kirigami shoe grip are illustrated. Through changing in the curvature of the shoe soles during walking, the spikes are activated (shown in the magnified view) to actively enhance the frictional properties between the shoe sole and walking surface, and reduce the risk of slips and falls.

Results

Design of kirigami metasurfaces for dynamic friction modulation

Our kirigami shoe grips are composed of a periodic array of needle-like spikes embedded in stainless steel sheets (with thickness 0.051 mm and Young's modulus E=193 GPa, **fig. S1**). We considered three different shapes for the cuts with concave, triangle, and convex spikes. Note that for a given cut shape, each kirigami pattern is characterized by two design parameters: the cut angle (γ), and the dimensionless ratio (δ/l) that defines the ratio between width of the ligaments separating the cuts (δ) and the characteristic length (l) of the periodic lattice (see the inset in **Fig. 2B**). By varying these two parameters, one can control the mechanical response of the kirigami patterns[22,28]. We then used non-linear finite element (FE) analyses (see "Numerical simulations" in Methods) to identify a kirigami patch that exhibits larger tilting angle (θ) and higher out-of-plane stiffness (K_{33}) for better engagement with the contacting surface while maintaining the actuated configuration of the kirigami patch under weight of the wearer.

In **Fig. 2A**, we report the numerical snapshots of unit cells with concave (left), triangle (middle), and convex (right) shaped cuts when subjected to in-plane uniaxial strain ε_{22}. We find that for all three patterns the applied deformation triggers a buckling instability that induces the buckling and pop-up of the spikes. For $20^o < \gamma < 60^o$ and $0.05 < \delta/l < 0.2$, we then monitored for each pattern the evolution of the out-of-plane tilting angle of the spikes (θ) as a function of the applied tensile strain ε_{22}. The data are reported in **Fig. 2B** demonstrating that the out-of-plane buckling results in an initial sharp increase in θ, and then an increasing regime followed by a plateau at higher strains. For example, for triangle spikes with $\gamma = 60^o$ and $0.05 < \delta/l < 0.2$, the tilting angle saturates at $\theta = 22^o$ for $\varepsilon_{22} \geq 0.1$. The maximum of average local strains in the shoe soles induced by changing the sole's curvature over a gait cycle (see the dashed line in **fig. S2**) is about $\varepsilon_{22} = 0.15$. At this strain range, we selected $\gamma = 30^o$ as a good candidate for cutting angle to achieve maximum tilting angle ($\theta \sim 30^o$) for all spike shapes (highlighted with blue dashed line in Fig. 2B).

Next, we constructed FE models of kirigami surfaces with different spike shapes at $\gamma = 30^o$ and $\delta/l = 0.05, 0.1, 0.15$ which are first stretched up to a typical maximum shoe sole's strain over a gait cycle ($\varepsilon_{22} = 0.15$) and then compressed in contact with a rigid plate to estimate the stiffness of spikes in the out-of-plane direction (K_{33}) (see "Numerical simulations" in Methods and Movie S2). The data are presented in **Fig. 2C**, which indicate that $\delta/l = 0.15$ results in maximum K_{33} across different levels of in-plane strain ε_{22} for all the shapes. Thus, having identified $\gamma = 30^o$

and $\delta/l = 0.15$ as ideal design parameters, we investigated the effect of spike shape on friction enhancement.

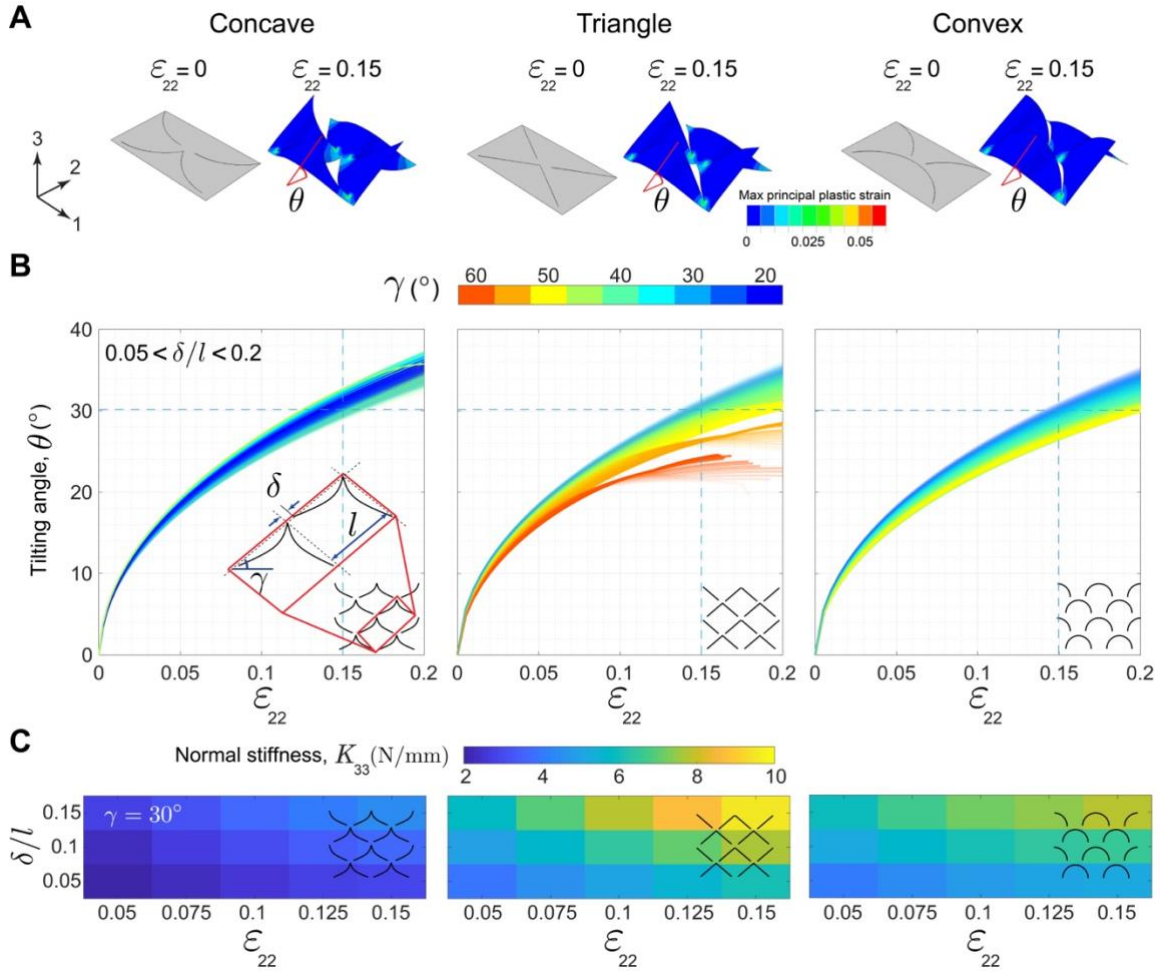

Fig 2. Mechanical characterization of the kirigami shoe grips with different spike shapes. (**A**) Numerical images showing the configurations of the kirigami unit cells with concave (left), triangle (middle), and convex (right) shapes at different levels of applied uniaxial strains, $\varepsilon_{22} = 0$, and 0.15. The colors represent the distribution of max principal plastic strains. (**B**) The tilting angle of the spikes (θ) were plotted as a function of ε_{22} for geometric design parameters γ and δ/l. The dashed lines correspond to $\varepsilon_{22} = 0.15$ (max average shoe sole's strain over a gait cycle) and $\theta \sim 30^{o}$(maximum tilting angle). (**C**) Effect of δ/l on the stiffness in 33-direction (K_{33}) of the kirigami spikes with concave, triangle, and convex shapes with $\gamma = 30_{o}$ as a function of ε_{22}.

In vitro mechanical characterization of kirigami shoe grips

Fig. 3A shows the undeformed (ε_{22}= 0) and buckled (ε_{22}= 0.15) configurations of the fabricated steel kirigami patches with $\gamma = 30^{o}$, $\delta/l = 0.15$, as well as concave, triangle, and convex spike shapes. These patches were manufactured by laser cutting stainless steel sheets (**fig. S3** and see "Fabrication of the kirigami patches" in Methods). A custom-built friction testing set-

up was retrofitted to a universal testing machine (Instron 5942 series) and used to evaluate the friction force between the kirigami prototypes and different surfaces (**fig. S4** and "Friction testing" in Methods).

In **Fig. 3B**, we reported the friction forces (F_f) between kirigami (prestretched at $\varepsilon_{22} = 0.15$) with different spike shapes and three common walking surfaces including ice (i.e., unmelted dry surface) (black solid lines), vinyl (blue solid lines), and hardwood (red solid lines) and compared the results with those measured for flat, spikeless steel control patches (dashed lines in Fig. 3B). The controls had the same thickness (0.051 mm) as the kirigami patches. Two primary friction responses were observed among all the patches and surfaces: (i) a smooth sliding in which the friction force starts with an initial peak (F_s) followed by a plateau (F_k), and (ii) a stick-slip response in which the friction force varies periodically between a maximum (F_s) and minimum (F_k) force, as schematically presented in the inset. The smooth sliding response was observed for hard surfaces such as wood and ice, where the kirigami spikes scratched against the surface with minimal penetration. The stick-slip response was observed for the semi-hard surface (vinyl), where the spikes appreciably penetrate the surface. Notably, the friction force-displacement curves for all the kirigami are greater than that of the flat spikeless control patches due to interactions (scratching or penetrating, confirmed by observing the surfaces after the tests) between the spikes and various surfaces, demonstrating the effectiveness of the kirigami patches in increasing sliding resistance.

Note that some degree of stick-slip friction was almost always observed between the kirigami and the test surfaces. For example, the triangle kirigami on ice exhibited a relatively low degree of stick-slip friction (black curve in Fig. 3B-middle), while almost all shapes on vinyl exhibited a pronounced degree of stick-slip friction (blue curves in Fig. 3B). This behavior is caused by penetration of the spikes into the test surfaces (stick events) resulting in static friction forces, followed by sharp drops caused by slip events when the force applied by the universal testing machine (equal to the friction force) is great enough to overcome the force of penetration and cause motion again. This is similar to plowing friction between a soft material and a harder one, where friction is caused by plowing asperities in the harder material through the softer one[39]. In our system, the kirigami spikes can be considered as very large asperities plowing through the softer surfaces such as vinyl. When the softer material accumulates at the tip of the spikes, the kirigami "sticks" until enough force is applied to fracture or slip over the accumulated material. However, plowing friction in general is not necessarily related to stick-slip friction; we mention plowing friction here more as an analog to the mechanism we believe is at play here.

We further quantified the ability of the kirigami patches to enhance sliding friction by comparing the coefficients of friction of the three walking surfaces to a flat, spikeless control surface as shown in **Fig. 3C**. The static coefficient of friction (before a slip event), denoted by μ_s, and kinetic coefficient of friction (during motion), denoted by μ_k, were estimated using $\mu_s = F_s/F_n$

and $\mu_k = F_k/F_n$, where F_n is the normal force acting on the patch. In the case of the smooth sliding, F_s is the peak friction force corresponds to static friction force that must be overcome before any sliding begins between two stationary surfaces, and F_k is the average kinetic friction force when the surfaces are in relative motion during shearing. For the stick-slip response, the static friction force (F_s) and kinetic friction force (F_k) are the maximum and the minimum magnitude of the measured friction forces, respectively[40, 41].

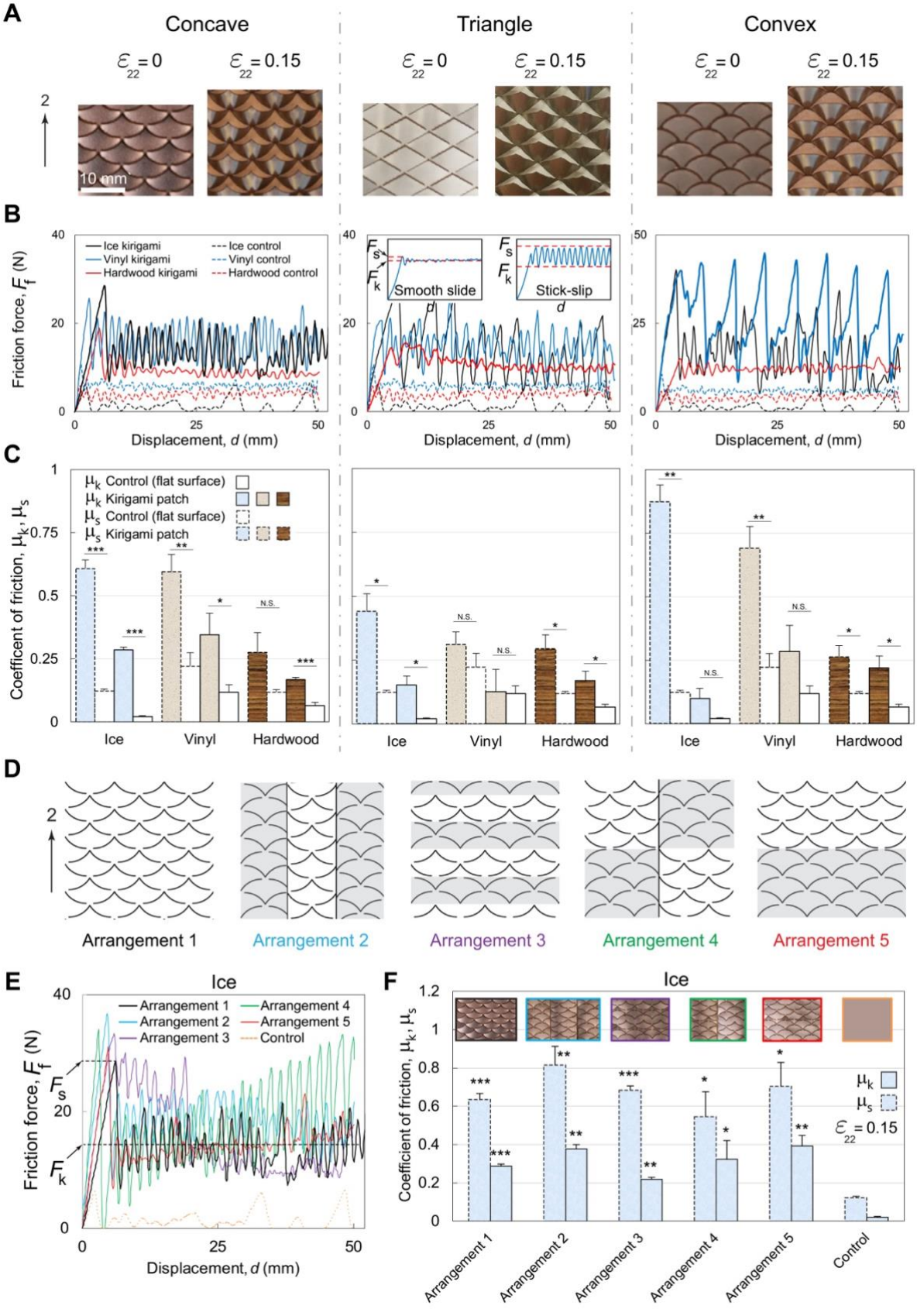
A
Concave
Triangle
Convex
$\varepsilon_{22} = 0$
$\varepsilon_{22} = 0.15$
2
10 mm
B
Friction force, F_f (N)
Ice kirigami
Vinyl kirigami
Hardwood kirigami
Ice control
Vinyl control
Hardwood control
F_s
F_k
Smooth slide
Stick-slip
Displacement, d (mm)
C
Coefficient of friction, μ_k, μ_s
μ_k Control (flat surface)
μ_k Kirigami patch
μ_s Control (flat surface)
μ_s Kirigami patch
N.S.
Ice
Vinyl
Hardwood
D
2
Arrangement 1
Arrangement 2
Arrangement 3
Arrangement 4
Arrangement 5
E
Ice
Arrangement 1
Arrangement 2
Arrangement 3
Arrangement 4
Arrangement 5
Control
Friction force, F_f (N)
F_s
F_k
Displacement, d (mm)
F
Ice
Coefficient of friction, μ_k, μ_s
μ_k
μ_s
$\varepsilon_{22} = 0.15$
Arrangement 1
Arrangement 2
Arrangement 3
Arrangement 4
Arrangement 5
Control

Fig 3. Friction enhancement of the kirigami shoe grips with various spike shapes and arrangements. (**A**) Experimental images showing the configurations of the fabricated steel kirigami patches (γ =30₀ and δ/l =0.15) with concave (left), triangle (middle), and convex (right) shapes at $\varepsilon_{22} = 0$ and 0.15. (**B**) Friction force (F_f) is measured for the kirigami patches with different spike shapes (solid lines) and flat control patches (dashed lines) on ice (black), vinyl (blue), and hardwood (red) surfaces. F_s and F_k are the static and kinetic friction forces. (**C**) Static and dynamic coefficients of friction (μ_s and μ_k) experimentally measured between the kirigami patches prestretched at $\varepsilon_{22} = 0.15$ with concave-, triangle-, and convex-shaped spikes as well as flat control patches, and ice, vinyl, and hardwood surfaces. (**D**) Schematics of kirigami patches with different spikes arrangements including arrangement 1 (unidirectional in black), arrangement 2 (3-column in blue), arrangement 3 (alternating rows in purple), arrangement 4 (checker in green), and arrangement 5 (mirror in red). (**E**) Friction force vs. displacement response of the concave kirigami patches with different spike arrangements and flat control surfaces (orange), sliding on ice. (**F**) Effect of different spike arrangements on static and dynamic friction coefficients (μ_s and μ_k) are reported on the right. The different arrangements of the fabricated grips are shown in the inset. Data reported as mean ± standard deviation for $n = 3$ measurements for each group. Two-sample t tests were used to determine the significance. *P < 0.05, **P < 0.01, ***P < 0.001, and N.S. not significant (kirigami patch versus flat control surface for both μ_s and μ_k).

We summarized the results in Fig. 3C, demonstrating significant improvement in both μ_s and $\mu_k$values for all the kirigami with various spike shapes compared with their respective controls (bare steel surfaces) across all the walking surfaces. This difference is especially dramatic in ice, where we see approximately an up to seven-fold enhancement in μ_s and fourteen-fold enhancement in μ_k. Interestingly, the triangular spikes exhibit the lowest improvement although they have the largest out-of-plane stiffness ($K_{33} = 11$ N/mm for $\delta/l = \varepsilon_{22} = 0.15$ - see the middle heat map in Fig. 2C); while the convex (broad and stiff geometry) and concave spikes (very sharp tip) exhibit higher friction enhancement. Importantly, the concave spikes showed the best performance on ice in maximizing kinetic friction coefficient from $\mu_k = 0.020$ to 0.285. Therefore, the concave spike was selected to manufacture the final kirigami prototypes and study the friction response of kirigami by arranging the spikes in different patterns and directions.

Kirigami shoe grips with varying arrangements of spikes

Next, the effect of spike arrangement on frictional properties of kirigami were experimentally investigated. We manufactured steel kirigami patches with five different spatial distributions of concave-shaped spikes including unidirectional (arrangement 1), 3-column (arrangement 2), alternating rows (arrangement 3), checker (arrangement 4), and mirror (arrangement 5), all illustrated in **Fig. 3D** and **fig. S5**. Similarly, we tested these by pulling the prestretched kirigami ($\varepsilon_{22} = 0.15$) on a test surface (see "Friction testing" in Methods). The friction force-displacement responses between the kirigami and ice with dry surface are presented in **Fig. 3E**. Interestingly, all the kirigami demonstrated enhanced frictional properties as compared to the control spikeless patch (orange dashed line), showing smooth sliding for ice (data for hardwood and vinyl surfaces

are presented in **fig. S6**). We also computed the friction coefficients for different kirigami arrangements, finding significant increases in μ_s (five-fold) and μ_k (fifteen-fold) on average for all the arrangements with respect to the control for ice (**Fig. 3F**). One could expect that the arrangement 1 should have the highest μ_s and μ_k values because all the spikes are pointing in the same direction, thereby dissipating the most possible energy for a fixed number of spikes because they should all be penetrating into the surface, yet this is not the case experimentally. This is due to a slight flattening of the spike tips as they are pressed against the surface, decreasing the ability of the forward-pointing spikes (i.e., pointing in the direction of displacement) to penetrate into the surface and making all arrangements have a similar friction response.

In vivo human force plate measurement of friction with kirigami shoe grip

To further support the capacity of the kirigami patches to modulate friction while walking, we conducted human gait experiments using a force plate. Three human subjects wore a kirigami patch on the soles of their shoes and walked across a force plate covered with a 1" thick layer of ice. Three orthogonal ground reaction forces exerted on the surface, F_x, F_y, and F_z, were concurrently recorded, illustrated in **Fig. 4A** (See "Experimental protocol for gait analysis (force plate test)" in Methods). The plot in Fig. 4A shows a typical gait response of walking over the first half of a gait cycle (i.e., stance phase that includes heel strike, support, and toe-off stages) in the x-direction. The response is characterized by a peak normal force in the z-direction, F_n equal to the weight of the human subject, and a small peak friction force in the x-direction within the weight acceptance stage (i.e., braking force), followed by a peak friction force in the negative x-direction within the toe-off stage (i.e., propulsion force denoted by F_s)[42,43].As expected, the force signal in the y-direction is approximately zero and negligible. Note that the kirigami shoe grips are designed to operate during the toe-off stage, where the bending of the shoes triggers the kirigami spikes to buckle out and engage with walking surfaces to increase friction.

In **Fig. 4B**, the variation of reaction forces in x- and z-directions for human subject 1 wearing kirigami shoe grip (arrangement 1) and a control flat sheet, as well as sneakers with grip and felt soles are presented. $F_n \cong 750$ N is the weight of the participant, which was recorded almost identical among all the tests. However, the peak friction force (F_s) has the highest value for the kirigami, and then it lowers for the sneakers and flat sheet, a signature of stronger friction enhancement of the kirigami shoe grip.

Note that the gait experiment represents a much more complex and dynamic system (unlike the quasi-static experiments of Figs. 3 and 4) and as such, the μ values were interpreted as an effective measure of slip resistance when walking rather than a widely applicable property of two surfaces. We defined a utilized coefficient of friction, μ, by normalizing the friction force with respect to the normal force, $\mu = F_s/F_n$. Five steel kirigami grips with different arrangements were evaluated in addition to a control flat sheet of the base material (**Fig. 4C**). Furthermore,

experiments using a 5° inclined ice surface (i.e., unmelted dry surface) mounted on the force plate were conducted to inform utilized coefficient of friction in this setting (see "Evaluation of utilized coefficient of friction on an inclined surface" in Supplementary Methods, and **fig. S7**). Additionally, gait evaluation was performed with a variety of commercial footwear ranging from winter boots to sneakers, loafers, and sandals with various tread groove patterns designed to increase the friction and provide a good grip to the person while walking with shoes (see the inset in Fig. 4C). Notably, all three human subjects exhibited average utilized friction coefficients in the range $0.22 < \bar{\mu} < 0.30$ on flat ice for all the spike arrangements, which on average is ten times more than that of the flat steel controls ($\bar{\mu} = 0.02$), and twice as large as the textured steel controls ($\bar{\mu} = 0.10$, purple column in Fig. 4C) and commercial shoes ($\bar{\mu} = 0.12$, grey column in Fig. 4C). The textured controls have the same thickness (0.051 mm) as the flat controls and kirigami patches (see "Fabrication of the kirigami patches" in Methods). The black columns are the experimental data recorded using the inclined surface, which represents the utilized coefficient of friction for the human subject 1 wearing steel kirigami patches with the varying arrangement of spikes on the soles of his shoes. The data show increased shear forces in *t*-direction for the inclined surface, results in growth between 10 to 20% in utilized friction coefficients with respect to the flat surfaces. These values were relatively consistent among all human subjects, supporting the ice-gripping capacity of kirigami shoe grips through dynamic friction modulation.

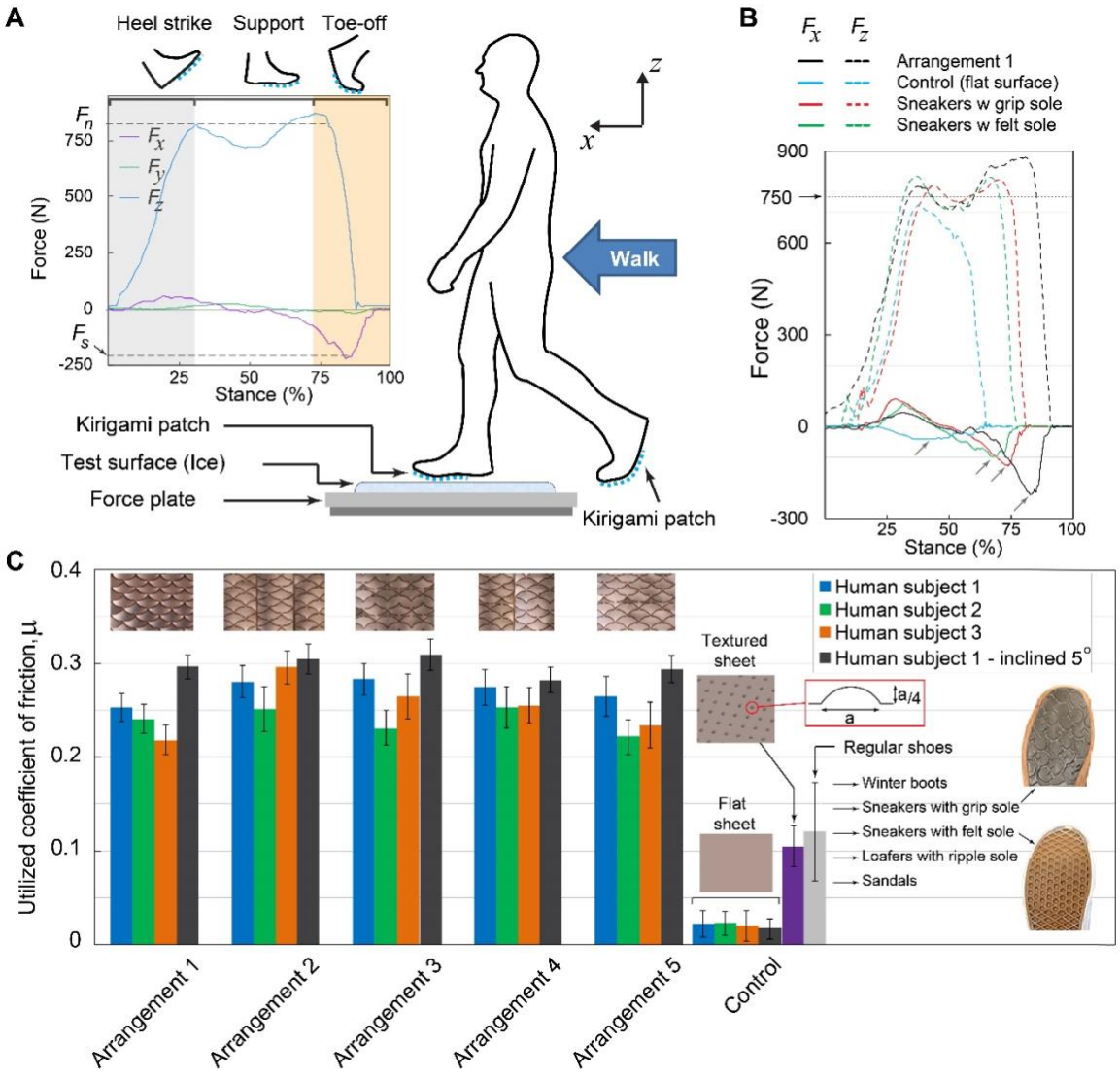

Fig 4. Kirigami shoe grip-induced changes in utilized friction coefficient on an ice surface. (**A**) Illustration of experimental setup used to measure the excreted forces to the ice walking surface over the stance phase that includes heel strike (weight acceptance), support (foot flat), and toe-off (propulsion). Ground reaction forces both in x-direction (friction force) and z-direction (human weight) were collected concurrently as participants walked on the force plate covered with ice. Peak normal force in the z-direction (F_n) and a peak friction force in the negative x-direction (F_s) are shown. Data were plotted as mean for $n = 10$ measurements. (**B**) Example of reaction forces, F_x (solid lines) and F_z (dashed line), recorded over a half gait cycle for human subject 1 wearing kirigami grip (arrangement 1 in black), control flat surface (blue), sneakers with grip soles (red), and sneakers with felt soles (green). The arrows point to the pick of propulsion reaction forces in x-direction (F_s). Data were plotted as mean for $n = 10$ measurements. (**C**) Utilized coefficient of friction (μ) reported for three human subjects shown in blue, green, and orange column bars. The experiments were carried out while the participants wearing the steel kirigami patches with different spike arrangements, the flat and textured control surfaces (shown in the inset), as well as various commercial shoes for the sake of comparison. The textured controls consist of an embossed pattern in the form of a square array of dimples raised against the surface (a=1 mm). The sneakers with grip and

felt soles are shown in the inset. Data reported as mean ± standard deviation for $n = 10$ measurements for each group.

Discussion

In summary, in view of the public health importance of reducing falls, we harness kirigami-based metasurfaces to mitigate slipping and falling. We demonstrate through attaching stretchable lightweight steel kirigami patches to the soles of shoes that we are able to actively enhance the frictional properties between the shoe soles and walking/working surfaces. In this work, we introduce several key elements including: (i) applying the change in the curvature of the shoe soles during commercial walking to dynamically actuate the kirigami shoe grips (i.e., without using any external source of energy), and (ii) reversible frequent shape transformation from flat surfaces (low friction) to 3D surfaces with popped up spikes (high friction) that enables us to tune friction dynamically (i.e., no need to remove the kirigami shoe grips). We present a systematic study by combining FE simulations and experimental methods to investigate the effect of kirigami meso-structure (geometry, shape, and arrangement of spikes) on frictional properties between the kirigami shoe grips and walking icy surfaces.

Notably, our proposed kirigami shoe grips are capable of enhancing lateral frictional properties that enable reducing the risk of slips and falls transversally to the direction of movement (i.e., biaxial friction enhancement). We observed that our symmetric kirigami pattern supports lateral friction force of a magnitude which is comparable to and even slightly larger than axial friction. Moreover, introducing asymmetry can further increase the lateral friction while axial friction remains in the same range (see "Kirigami shoe grips with biaxial friction control" in Supplementary Information, and **fig. S8**). This simple demonstration confirms that buckling-induced kirigami is a rich platform with promising future directions, and can be used to tune frictional properties of patterned surfaces. This design can be expanded by introducing curvilinear grids to have a more pronounced change in the orientation of the spikes in lateral directions which requires further studies.

The typical walk consists of a repeated gait cycle that contains two phases: (i) a first half cycle (stance phase) that can be dived into three stages: heel strike (weight acceptance), support (foot flat), and toe-off (propulsion); and (ii) a second half cycle (swing phase) that includes leg lift and forward motion. The kirigami metasurfaces are designed to operate during the propulsion stage, where the bending of the shoes induces stretching strain along the soles to activate the kirigami and generates higher friction forces in the forefoot. However, slipping during weight acceptance after heel contact (approximately 0-20% stance phase) is more hazardous compared to slipping during push-off. During the acceptance phase (from heel contact to foot flat), shoes are not significantly bent and the effect of increasing friction due to deformation of the kirigami metasurfaces may not be achieved. Thus, this point is a limitation in this study and potential area

of future slip-resistance. However, the finite residual deformation (i.e., slight localized plastic strains at the hinges) caused by deformation of patches results in a surface which is not fully smooth at rest position and can be beneficial to increase the friction of unactuated patches over foot flat and toe-off stages (see "Effect of material behavior on the response of kirigami shoe grips" in Supplementary Information). The current kirigami grips cover only the top half of the sole. Therefore, the braking forces – generated from the interaction between the heel region of the shoe sole and ice in the weight acceptance phase of gait – cannot be controlled and may vary for shoes made of various materials and sole groove patterns. Moreover, attachment of the kirigami grips may change the gait of human subjects and affects the braking forces. Therefore, to achieve further friction improvement over all the stages of stance, we can make outsoles that cover the entire sole and consists of two portions: (i) the top portion consists of the kirigami pattern made of textured sheets to increase the friction in the push-off stage; and (ii) the bottom portion (heel region) made of dimpled or tread groove patterns (no kirigami pattern) to generate higher braking forces and increase friction in the weight-acceptance phase and finally reduce the risk of slip[44-46].

The proposed approach could be potentially beneficial to reduce the risk of slip and fall for other slippery surfaces including oily or wet hardwood floors and vinyl. The tribological mechanisms behind the kirigami patches could be further assessed with more detailed wear studies (e.g., estimating wear volume through scratch depth in test surfaces and measuring wear life) and *in situ* monitoring of the kirigami during tests to assess the degree of tip flattening and potentially plowing. The stainless steel prototypes were employed to demonstrate the ability of kirigami surfaces for dynamic modulation of friction. Future development will include further evaluation of materials including composites for field application. For example, they could be designed as a bilayer composite: a body made of a high-stiffness elastomer with microfeatures (e.g., dimple, groove) and steel reinforced spiked tips. The Elastic body with grooves provides friction in the range of commercially-available winter shoes or anti-slip solutions[47, 48], and the kirigami spikes provide extra friction enhancement through dynamic orienting. This can improve the life time of steel shoe grips under cycling loads (see "Experimental fatigue testing of the kirigami shoe grips" in Supplementary Information, and fig. S9). Future successful translation of these technologies will involve further human dynamic evaluation across all the stages of stance[49-51] and ambulation in ice containing environments including inclined surfaces[52, 53]. We envision morphable kirigami patches could be customized to the shape of person's specific shoe soles by introducing functional gradient in size and shape of spikes to provide required friction force during daily activities.

Methods

Numerical simulations

The simulations were carried out using the commercial Finite Element (FE) package ABAQUS 2019 (SIMULIA, Providence, RI). The Abaqus/Standard solver was employed for all simulations. In all our analyses we discretize the sheets using four-node general-purpose shell elements with reduced integration and hourglass control (S4R Abaqus element type) and, guided by our experiments, model the cuts as elongated rectangular voids with width of 0.1 mm. Since plasticity has little effect on the observed phenomena (see "Effect of material behavior on the response of kirigami shoe grips" in Supplementary Information, and **fig. S10**), the material behavior of the steel sheets is captured using a linear elastic material model with an elastic Young's modulus E = 193 GPa and a Poisson's ratio $\nu = 0.27$. To reduce the computational cost and ensure the response of the system is not dominated by boundary effects, we conducted analysis on unit cells subjected to periodic boundary conditions applied on opposite edges. Note that in the finite size structures, the response is slightly affected by the effect of the boundaries, and the morphology and characteristics of the emerging 3D pop-ups (e.g. relation between tilting angle and applied strain) are found to be unaltered (see "Stress-strain response of finite size kirigami under uniaxial tension" in Supplementary Information, and **fig. S11**). Two sets of analyses were performed:

Deformation of kirigami patches under uniaxial in-plane tensile strain

The uniaxial response of the kirigami structures was simulated in two steps: (i) a linear perturbation analysis (*BUCKLE module in Abaqus) was used to identify the critical buckling mode; (ii) the non-linear post-buckling response of the systems was simulated by introducing a small imperfection (~0.005l) in the form of the critical mode into the initial geometry and conducting static analysis (*STATIC module in Abaqus).

Examining the normal stiffness of the spikes

Following uniaxial tensile simulation of kirigami patches, the normal stiffness of buckled spikes was examined by subsequent compression of pre-stretched patches using a rigid plate while the displacement of four corners of the unit cells were constrained in normal direction. The plate was discretized using rigid shell elements and was initially positioned slightly above the tip of the spikes, which were calculated from previous uniaxial tensile simulations. We performed dynamic implicit analysis (*DYNAMIC module in Abaqus) by lowering the plate until it pushed the spikes down for 0.25 mm. A simplified contact law (General Contact type interaction) was assigned to the model with a hard contact for normal behavior and a frictionless tangential behavior. The reaction force of the plate was recorded as a function of applied displacement in the normal direction (**fig. S12**). Finally, the normal stiffness was given by calculating the initial slope of the force-displacement curve.

ABAQUS scripts used for the above-mentioned analyses are provided in Supplementary Information.

Fabrication of the kirigami patches

The metal kirigami patches were fabricated from 0.051 mm thick 301 stainless steel shim stock (Rockwell hardness C32, Trinity Brand Industries, McMaster-Carr part# 2316K11) and laser cut using a Kern MICRO equipped with a 150 W laser. The dimension of the kirigami patches is 11 × 7 cm with 160 stretchable spikes, shown in fig. S1A. The spikes are fabricated in different shapes including concave, triangle, and convex (fig. S1B). Finally, the fabricated kirigami patches in the undeformed (ε_{22}= 0) and stretched (ε_{22}= 0.2) configurations with various spike shapes and arrangements including unidirectional, mirror, alternating rows, 3-column, and checker are shown in figs. S3 and S5. Both the flat and textured control patches were made of the same 301 stainless steel sheets with thickness 0.051 mm, Rockwell hardness C32, and dimension 11 × 7 cm. The textured controls were manufactured using a custom-made embossing hammer to create an embossed pattern consists of a square array of dimples with periodicity length of 5 mm (see the inset in Fig. 4C), which is raised against the surface of the flat sheet (a=1 mm).

Friction testing; experimental set-up

Friction testing was carried out using a custom attachment designed in-house for an Instron 5942 series Universal Testing System with a 500 N load cell, shown in fig. S4. The attachment consists of a weighted sled, a table on which the sled slides, and an M4 eyebolt which attaches to the crosshead of the testing machine and pulls the sled at a constant velocity of 10 mm/s via a cotton twine string. The table is 600 mm long and 150 mm wide made from a 1/4” thick acrylic sheet. It has four 6 mm holes, which allow it to be screwed onto the base of the testing machine and a screw-mounted pulley (McMaster-Carr, part# 3071T7) for the string. In addition, the table has two M6 tapped holes for 300 mm long threaded rods (McMaster-Carr, part# 93325A418) which support the weight of the table extending off the base. The sled is 165 mm long and 97 mm wide made from two 1/4” acrylic sheets stacked and held together by M4 screws. The top sheet functions as a barrier to prevent the weight from sliding off the top of the sled. Finally, it has an M4 eyebolt screwed to the front for the string, which is tied on both ends using a bowline knot.

To study the effects of spike shape and arrangement on the friction response of the patches, three shapes (“concave”, “triangle”, and “convex”) with five arrangements (“unidirectional”, “mirror”, “alternating rows”, “3-column”, and “checker”) each were tested for a total of 15 different patches and one control patch (i.e., flat sheet of stainless steel). Three different surfaces were tested: hardwood (Armstrong Flooring, item # FP735WEAS502C14), vinyl (Armstrong Flooring, item #FP84660159), and ice, which was made in-house by freezing water in -20 °C freezer in a 34.3 × 24.4 × 7.0 cm aluminium tray overnight.

The patches were clamped to the sled to strain them to approximately 15%, and a 5 kg weight was placed on top. The sled was pulled at a constant velocity of 10 mm/s until reaching the end of the surface, resulting in a plot of (friction) force against extension. This was repeated five times per patch.

Experimental protocol for gait analysis (force plate test)

Force plate tests were carried out using an AMTI AccuGait Optimized™ force plate connected to a PC running the NetForce™ data acquisition software. Three healthy adults (two men and one woman, age 24.6±5.2 years; mass 75.0±14.7 kg; height 172±12 cm; US shoe size 9.3±1.7; mean ± SD) participated in the study. The study was approved by the Massachusetts Institute of Technology Committee on the Use of Humans as Experimental Subjects (MIT COUHES) and carried out according only to the approved methods. The nature of the study, including its minimal risks, were explained to the participants, who then provided written consent to participate in the study. Participants were provided with a safety helmet, knee and elbow pads, and access to a hand rail.

One surface, ice, and six different metal patches were tested: concave-shaped spikes with five arrangements ("unidirectional", "mirror", "alternating rows", "3-column", and "checker") each. Six controls were tested: a flat steel sheet attached to the shoe sole (i.e., no kirigami pattern), and five commercial shoes (no patch) including winter boots, sneakers with grip soles, sneakers with felt soles, loafers with ripper soles, and sandals. The ice surface was mounted on top of the 51×51 cm force plate. The ice was at -20 °C (unmelted dry surface from the freezer) upon beginning the test, which provided ample time for the participants to perform the test before the ice started melting. In cases where the ice was visibly scratched or started melting between tests, the ice was replaced before continuing with the tests, as multiple ice blocks were frozen and prepared for the experiment (variation of ice surface temperature shown in **fig. S13**). Each patch was attached to the participants' shoe on their dominant foot by fixing both ends using duct tape to cover the top half of the sole. The participants then walked forward one step and then stepped on the force plate 10 times per patch. The step length and speed were not regulated. Each repeat resulted in a plot of three orthogonal forces and moments (in x-, y-, and z-directions), of which only the directions corresponding to the normal (human weight) and friction forces were used, shown in Fig. 4A.

References

1. National Safety Council. Injury Facts. (2017). Available at: https://injuryfacts.nsc.org/.
2. Li, K., Courtney, T. & Huang, Y. Slipping and falling experience and perception of floor slipperiness: A field survey in 10 fast-food restaurants in Taiwan. *Prof. Saf.* 51, 34–38 (2006).
3. Morrison, R., Chassin, M. & Siu, A. The medical consultant's role in caring for patients with hip fracture. *Ann. Intern. Med.* 128, 1010–1020 (1998).
4. Wolinsky, F. D., Fitzgerald, J. F. & Stump, T. E. The effect of HIP fracture on mortality, hospitalization, and functional status: A prospective study. *Am. J. Public Health* 87, 398–403 (1997).
5. J., P. *et al.* Mortality and cause of death in hip fracture patients aged 65 or older - A population-based study. *BMC Musculoskelet. Disord.* 12, 2–7 (2011).
6. LeBlanc, E. S. *et al.* Hip fracture and increased short-term but not long-term mortality in healthy older women. *Arch. Intern. Med.* 171, 1831–1837 (2011).
7. Tinetti, M. E. *et al.* A multifactorial intervention to reduce the risk of falling among elderly people living in the community. *N. Engl. J. Med.* 331, 821–827 (1994).
8. Englander, F., Hodson, T. & Terregrossa, R. Economic dimensions of slip and fall injuries. *J. Forensic Sci.* 41, 733–746 (1996).
9. Hsu, J. *et al.* Slip resistance of winter footwear on snow and ice measured using maximum achievable incline. *Ergonomics* 59, 717–728 (2016).
10. Stevens, J. A., Corso, P. S., Finkelstein, E. A. & Miller, T. R. The costs of fatal and non-fatal falls among older adults. *Inj. Prev.* 12, 290–295 (2006).
11. Bureau of Labor Statistics, U.S. Department of Labor, *The Economics Daily*, 42,480 work injuries involved ice, sleet, or snow 2014 (visited *September 24, 2019*).
12. Chang, W. R., Leclercq, S., Lockhart, T. E. & Haslam, R. State of science: occupational slips, trips and falls on the same level. *Ergonomics* 59, 861–883 (2016).
13. Hanson, J. P., Redfern, M. S. & Mazumdar, M. Predicting slips and falls considering required and available friction. *Ergonomics* 42, 1619–1633 (1999).
14. Gao, C. & Abeysekera, J. A systems perspective of slip and fall accidents on icy and snowy surfaces. *Ergonomics* 47, 573–598 (2004).
15. Gao, C., Holmér, I. & Abeysekera, J. Slips and falls in a cold climate: Underfoot surface, footwear design and worker preferences for preventive measures. *Appl. Ergon.* 39, 385–391 (2008).
16. Bruce, M., Jones, C. & Manning, D. P. Slip-resistance on icy surfaces of shoes, crampons and chains - a new machine. *J. Occup. Accid.* 7, 273–283 (1986).
17. Gard, G. & Berggård, G. Assessment of anti-slip devices from healthy individuals in different ages walking on slippery surfaces. *Appl. Ergon.* 37, 177–186 (2006).
18. Berggård, G. & Johansson, C. Pedestrians in wintertime - Effects of using anti-slip devices. *Accid. Anal. Prev.* 42, 1199–1204 (2010).
19. Gao, C., Abeysekera, J., Hirvonen, M. & Grönqvist, R. Slip resistant properties of footwear on ice. *Ergonomics* 47, 710–716 (2004).
20. Menant, J. C., Steele, J. R., Menz, H. B., Munro, B. J. & Lord, S. R. Optimizing footwear for older people at risk of falls. *J. Rehabil. Res. Dev.* 45, 1167–1181 (2008).
21. Blees, M. K. *et al.* Graphene kirigami. *Nature* 524, 204–207 (2015).
22. Rafsanjani, A. & Bertoldi, K. Buckling-Induced Kirigami. *Phys. Rev. Lett.* 118, 1–11

(2017).
23. Tang, Y. *et al.* Programmable Kiri-Kirigami Metamaterials. *Adv. Mater.* 29, 1–9 (2017).
24. Zhang, Y. *et al.* A mechanically driven form of Kirigami as a route to 3D mesostructures in micro/nanomembranes. *Proc. Natl. Acad. Sci.* 112, 11757–11764 (2015).
25. Liu, Z. *et al.* Nano-kirigami with giant optical chirality: supplementary material. *Sci. Adv.* 4, 1–8 (2018).
26. Wu, C., Wang, X., Lin, L., Guo, H. & Wang, Z. L. Paper-Based Triboelectric Nanogenerators Made of Stretchable Interlocking Kirigami Patterns. *ACS Nano* 10, 4652–4659 (2016).
27. Jang, N. S. *et al.* Simple Approach to High-Performance Stretchable Heaters Based on Kirigami Patterning of Conductive Paper for Wearable Thermotherapy Applications. *ACS Appl. Mater. Interfaces* 9, 19612–19621 (2017).
28. Rafsanjani, A., Zhang, Y., Liu, B., Rubinstein, S. M. & Bertoldi, K. Kirigami skins make a simple soft actuator crawl. *Sci. Robot.* 3, eaar7555 (2018).
29. Dias, M. A. *et al.* Kirigami actuators. *Soft Matter* 13, 9087–9092 (2017).
30. Zheng, W. *et al.* Kirigami-Inspired Highly Stretchable Nanoscale Devices Using Multidimensional Deformation of Monolayer MoS 2. *Chem. Mater.* 30, 6063–6070 (2018).
31. Morikawa, Y. *et al.* Ultrastretchable kirigami bioprobes. *Adv. Healthc. Mater.* 7, 1–10 (2018).
32. Shyu, T. C. *et al.* A kirigami approach to engineering elasticity in nanocomposites through patterned defects. *Nat. Mater.* 14, 785–789 (2015).
33. Ma, R., Wu, C., Wang, Z. L. & Tsukruk, V. V. Pop-Up Conducting Large-Area Biographene Kirigami. *ACS Nano* 12, 9714–9720 (2018).
34. Song, Z. *et al.* Kirigami-based stretchable lithium-ion batteries. *Sci. Rep.* 5, 1–9 (2015).
35. Wilson, A. M. *et al.* Locomotion dynamics of hunting in wild cheetahs. *Nature* 498, 185–189 (2013).
36. Skutch, A. F. *Helpers At Birds' Nests: Cooperative Breeding & Related Behaviour* (University of Iowa Press, 1999).
37. Marvi, H. & Hu, D. L. Friction enhancement in concertina locomotion of snakes. *J. of the Royal Society Interface* 9, 3067–3080 (2012).
38. Guo, Z. V. & Mahadevan, L. Limbless undulatory propulsion on land. *Proc. Natl. Acad. Sci.* 105, 3179–3184 (2008).
39. Suh, N. P. & Sin, H.-C. The Genesis of Friction. *Wear* 69, 91-114 (1981).
40. Lee, D. W., Banquy X. & Israelachvili, J. N. Stick-slip friction and wear of articular joints. *Proc. Natl. Acad. Sci.* 110, 567–574 (2013).
41. Das, S. *et al.* Stick–slip friction of gecko-mimetic flaps on smooth and rough surfaces. *J. R. Soc. Interface* 12, 20141346 (2015).
42. Giakas, G. & Baltzopoulos, V. Time and frequency domain analysis of ground reaction forces during walking: an investigation of variability and symmetry. *Gait & Posture* 5, 189-197 (1997).
43. Lieberman, D. E. *et al.* Foot strike patterns and collision forces in habitually barefoot versus shod runners. *Nature* 463, 531–535 (2010).
44. Li, K.W. *et al.* The effect of shoe sole tread groove depth on the friction coefficient with different tread groove widths, floors and contaminants. *Appl. Ergon.* 37, 743-748(2006).
45. Yamaguchi, T. & Hokkirigawa, K. Development of a high slip-resistant footwear outsole using a hybrid rubber surface pattern. *Ind. Health* 52, 414-423 (2014).

46. Yamaguchi, T. *et al.* Efficacy of a rubber outsole with a hybrid surface pattern for preventing slips on icy surfaces. *Appl. Ergon.* 51, 9-17(2015).
47. Rizvi, R., Naguib, H., Fernie, G., & Dutta, T. High friction on ice provided by elastomeric fiber composites with textured surfaces. *Appl. Phys. Lett.* 106, 111601 (2015).
48. Ion, A., Kovacs, R., Schneider, O., Lopez, P., & Baudisch, P. Metamaterial Textures. *Proceedings of CHI Conference on Human Factors in Computing Systems* 336 (2018).
49. Iraqi, A., Cham, R., Redfern, M. S., Vidic, N. S., & Beschorner, K. E. Kinematics and kinetics of the shoe during human slips. *J. Biomech.* 74, 57-63 (2018).
50. McGorry, R. W., Chang, C. C., & DiDomenico, A. Rearward movement of the heel at heel strike. *Applied Ergonomics* 39, 678-684 (2008).
51. Powers, C. M., Blanchette, M. G., Brault, J. R., Flynn, J., & Siegmund, G. P. Validation of walkway tribometers: establishing a reference standard. *J Forensic Sci.* 55, 366-370 (2010).
52. Hsu, J., Li, Y., Dutta, T. & Fernie, G. Assessing the performance of winter footwear using a new maximum achievable incline method. *Applied Ergonomics* 50, 218-225 (2015).
53. Hsu, J., Shaw, R., Novak, A., Li, Y., Ormerod, M., Newton, R., Dutta, T. & Fernie, G. Slip resistance of winter footwear on snow and ice measured using maximum achievable incline. *Ergonomics* 59, 717-728 (2016).

Acknowledgements: We would like to thank Tiffany Hua, Mache Cruz, Nicoletta Inverardi, Xiaoya Lu, and Vance Soares for their help with experimental studies, Stan Cotreau, Chris Haynes, and Adam Wentworth for the help with manufacturing the experimental specimens, and Prof. R. Langer for fruitful discussions. **Funding:** This work was funded in part by a startup grant from the Department of Mechanical Engineering, MIT (G.T.). K.B. acknowledges support by National Science Foundation under awards DMR-1420570 (Materials Research Science and Engineering Center) and EFRI C3 SoRo 1830896. A.R. acknowledges support from Swiss National Science Foundation Grant P300P2-164648. Disclosures: K.B. is a co-inventor on a patent application describing kirigami systems. S.B., S.P., A.R., K.B., and G.T. are co-inventors on a provisional patent application for the technology described. Complete details of all for profit and not for profit relationship of G. Traverso can be found at the following link: https://www.dropbox.com/sh/szi7vnr4a2ajb56/AABs5N5i0q9AfT1IqIJAE-T5a?dl=0. The remaining authors disclose no conflicts.

Data availability: The authors declare that the main data supporting the results in this study are available within the paper and its Supplementary Information. ABAQUS scripts used for the numerical analyses are provided in supplementary materials.

Supplementary Information for

Kirigami Metasurfaces for Bioinspired Assistive Shoe Grips

Sahab Babaee, Simo Pajovic, Ahmad Rafsanjani, Yichao Shi, Katia Bertoldi, Giovanni Traverso

This file includes:

Supplementary Notes

Evaluation of utilized coefficient of friction on an inclined surface

We have conducted further experiments to evaluate utilized coefficient of friction using an inclined surface. The ice surface was mounted on top of the 51×51 cm force plate with an ascending inclined angle, $\theta = 5^{\circ}$ (Fig. S7). F_x and F_z are the ground reaction forces in x- and z-directions recorded by the force plate during walking over the half of a gait cycle. The utilized coefficient of friction (μ) was then calculated by:

$$\mu = \frac{F_t}{F_n} = \frac{F_x cos\theta + F_z sin\theta}{F_z cos\theta - F_x sin\theta}$$

, where F_t and F_n are the reaction forces in *t*- and *n*-directions. The detailed protocol of gait trials and instruction to the subject for walking on the inclined surface were the same as flat surfaces, described in the Methods section.

Kirigami shoe grips with biaxial friction control

Fig. S8A shows the design of two triangle kirigami structures with symmetric and asymmetric arrays of spikes. In the asymmetric design, the rows of tips of each spike are alternately shifted by the quarter of the unit cell's width to the right and left. We prototyped the kirigami out of 0.127 mm thick polyester plastic shim stock (Artus Corporation, NJ), and performed friction tests using the custom-built friction set-up (see fig. S4 and "Friction testing" in Methods). The kirigami were stretched $\varepsilon_{22} = 0.15$ in 2-direction (Fig. S8B) that results in buckling out of the spikes, and then clamped to the sled with 5 kg weight on the top. The sled was pulled at a constant velocity of 10 mm/s in the 2-direction until reaching the end of the hardwood surface. Then, to evaluate the friction forces in the lateral direction, we repeated the same test by pulling the sled in the 1-direction. In Fig. S8C, we reported the friction forces (F_f) between kirigami (prestretched at $\varepsilon_{22} = 0.15$) with symmetric (left plot) and asymmetric (right plot) arrays of spikes and a hardwood surface as a function of displacement. F_f^1 and F_f^2 are the recorded friction forces in the 1- and 2-directions, shown by dashed and solid lines, respectively. Each test was performed three times with the new kirigami, shown by different colors in Fig. S8C. Interestingly, the data demonstrates that not only both kirigami are capable of biaxial friction enhancement, but also the friction forces in the lateral direction (F_f^1) are higher than the forces in the axial direction (F_f^2). This lateral friction enhancement is even more pronounced for the asymmetric kirigami design.

Experimental fatigue testing of the kirigami shoe grips

We carried out fatigue testing to predict the life of steel shoe grips under cyclic tensile loads. An Instron 5942 series Universal Testing System with a 500 N load cell was used to apply cyclic uniaxial loading under strain-controlled conditions to the specimens (kirigami structures). A 2.5 mm thick ice block (300 ×120 mm) was mounted with the dry surface in a vertical orientation in contact with the kirigami surfaces such that the tips of the kirigami spikes scratched the ice block while the top crosshead of the testing machine pulled or pushed the kirigami. All tests were conducted using a trapezoidal waveform with $\varepsilon_{Applied}^{max} = 0.15$, shown in Fig. S9. To determine the fatigue life, the specimen failure was defined at the point when a 50% drop in the maximum load (compared to the first cycle) or rupture is recorded. In Fig. S9, we reported the peak force in each cycle, F_{max}, versus the number of loading cycles, n, for the kirigami structures with concave, triangle, and convex spike shapes. We found that the concave kirigami prototypes fail at $n{\sim}1700$ cycles, while the triangle and convex kirigami fail at $n{\sim}1100$ and $n{\sim}900$ cycles, respectively.

Effect of material behavior on the response of kirigami shoe grips

We examined the effect of plasticity and investigated the response of both elastic and elastoplastic kirigami structures under uniaxial tensile loads. We performed FE simulations by assuming an elastic-perfectly plastic material model (with yield stress $\sigma_y = 759$ MPa for 301 stainless steel) under cyclic loading (5 cycles), and compared the results to those obtained for purely elastic kirigami sheets. The results reported in Fig. S10 are for steel kirigami patches with concave, triangle, and convex spike shapes characterized by $\gamma = 30^{o}$, $\delta/l = 0.15$. Our finding suggests that while the effective stress-strain response of kirigami patches is affected by plasticity beyond out-of-plane buckling regime (Fig. S10A), the plastic strains localized in the hinges are moderate and the residual macroscopic strain is below 2% for all three patterns (Fig. S10B). From a practical point of view, this residual deformation can be beneficial since it potentially increases the friction of unactuated patches. Moreover, the effect of plasticity on tilting angle of kirigami sheets is negligible (Fig. S10C). Although the residual deformations caused by plasticity at the hinges are inevitable, the plastic deformation does not affect the morphology of the emerging 3D pop-ups, as their characteristics e.g. relation between tilting angle and applied strain are found to be unaltered.

Stress-strain response of finite size kirigami under uniaxial tension

We performed finite size simulations for kirigami structures with triangular cut pattern comprised of 16×2, 16×4, 16×6, 16×8 units and compared the results with those obtained from periodic boundary conditions (PBC). For kirigami structures, three deformation regimes are identified: (i) initial linear regime, (ii) out of plane buckling and departure from linearity, and (iii) hardening due to stretching of the hinges. As shown in Fig. S11, the linear regime is similar for all the samples due to in-plane deformation. By increasing the number of unit cells, the critical strain at which the out-of-plane buckling initiates becomes closer to the response of PBC. On the other hand, increasing the number of horizontal unit cells results in constraining more units at the

boundaries, which affects the hardening regime. Therefore, through the application of periodic boundary conditions, we avoid the dependency of the presented results on the choice of the number of units and save computational costs. We confirm that for real applications, the periodic boundary condition can be used as a guide while the results of finite size models should also be considered in the final prototypes.

Supplementary Figures

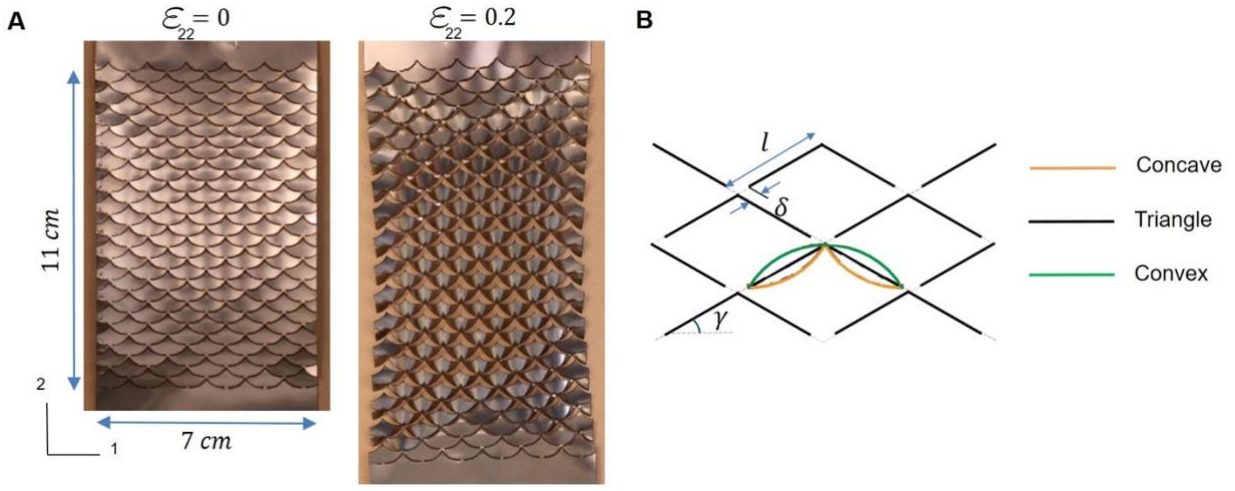

Figure S1: Fabricated steel kirigami shoe grips. (**A**) Undeformed (ε_{22}= 0) and stretched (ε_{22}= 0.2) configurations of the stainless steel kirigami patch made of a periodic array of concave-shaped spikes perforated in one direction. (**B**) The schematics of different spike shapes (in the middle) including concave (orange), triangle (black), and convex (green) with identical cut-angle ($\gamma = 30^o$) and hinge over cut-length ratio ($\delta/l = 0.15$).

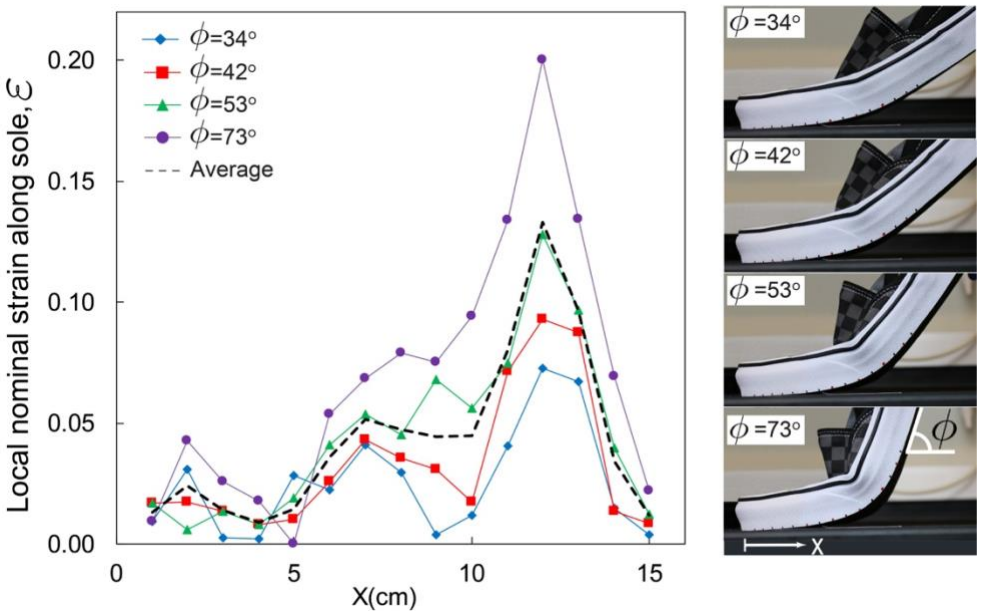

Figure S2: Distribution of strains along a shoe sole over a half gait cycle. The local strains, ε, were reported for different angles between the shoe sole and the walking surface ($\varphi = 34^o$ (blue), 42^o (red), 53^o(green), and 73^o (purple)) as a function of distance (x) from the shop tip. The snapshots showing the shape of the shoe at the different angles are illustrated on the right.

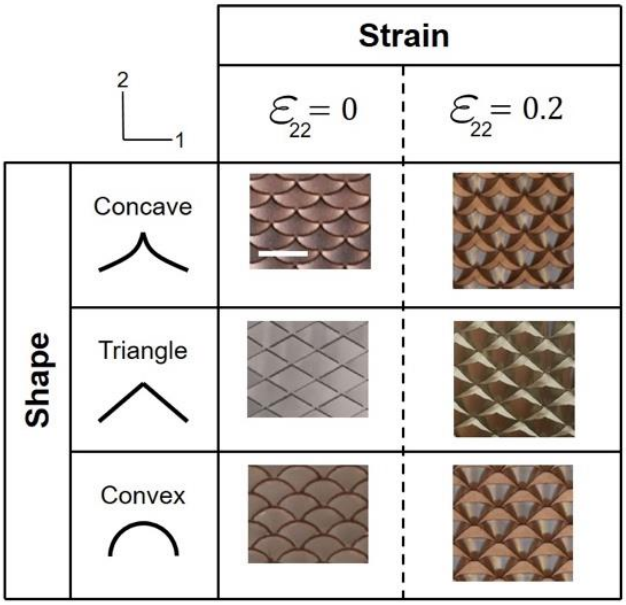

Figure S3: Fabricated kirigami shoe grips with different spike shapes. Undeformed (ε_{22}= 0) and stretched (ε_{22}= 0.2) configurations of the stainless steel kirigami patches with different spike shapes including concave, triangle, and convex that were considered for this study. Scale bar is 10 mm.

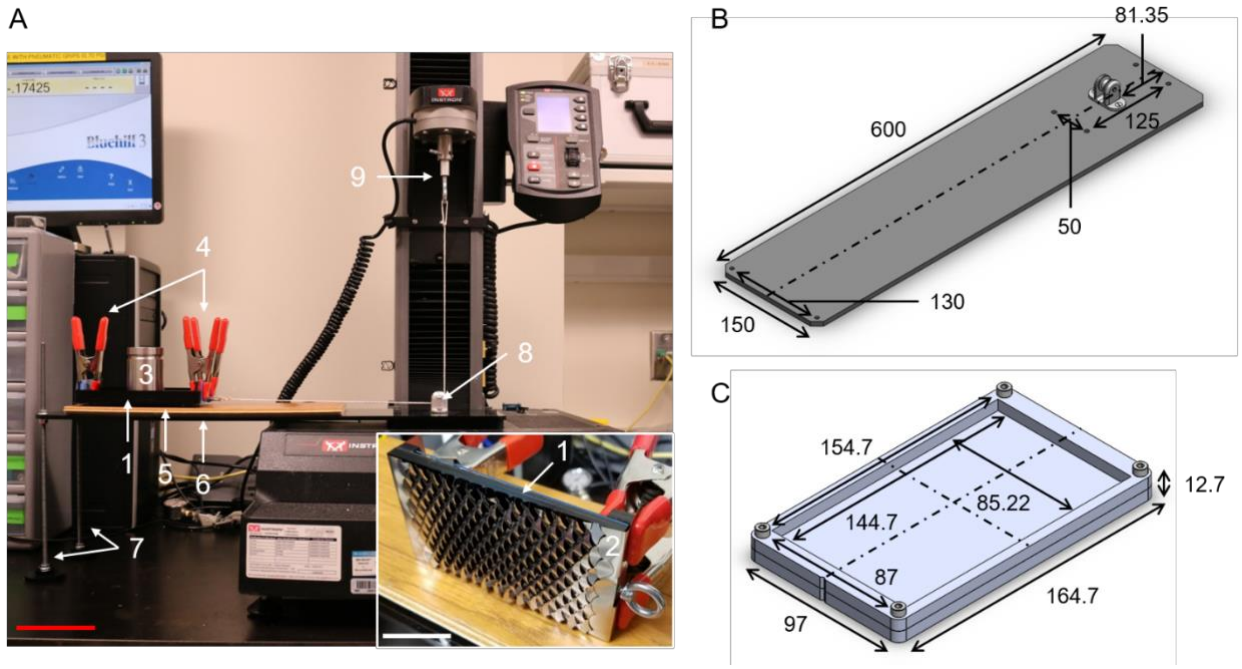

Figure S4: Friction testing set-up. (**A**) A universal testing machine (Instron 5942 series) with a 500 N load cell was used to evaluate the friction properties of the kirigami patches for various surfaces. The set-up (side view in the image) includes: (1) friction testing sled (bottom side shown in inset image) (2) kirigami patch, (3) weight, (4) clamps used to secure kirigami patch in the deformed state at 0.2 strain, (5) test surface (e.g., wood), (6) friction testing table, (7) M6 threaded rods used to support friction testing table, (8) low-friction pulley, and (9) hook attachment for crosshead to pull sled. Red scale bar is 100 mm; white scale bar in inset is 20 mm. The inset image is a bottom view of the friction testing sled with the kirigami patch attached. (1) and (2) are consistent with the outer image. The CAD model of the friction testing table (6) and sled without a kirigami patch (1) are illustrated in an isometric view in (**B**) and (**C**), respectively. All dimensions are in mm.

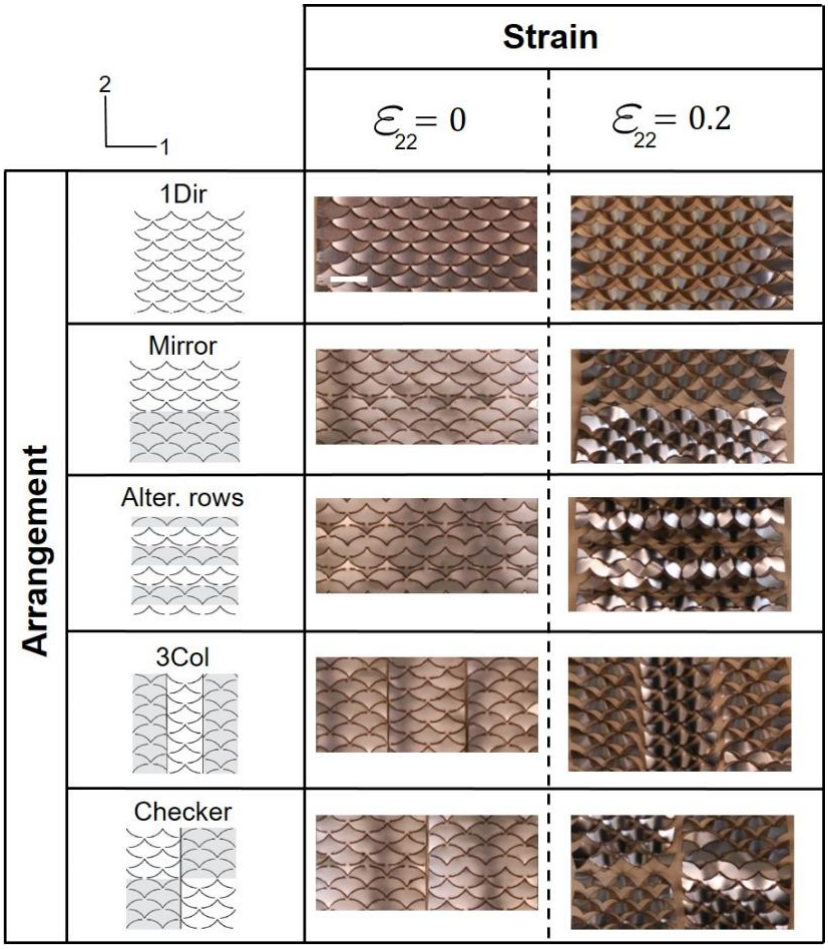

Figure S5: Fabricated steel kirigami shoe grips with different spike arrangements. Undeformed (ε_{22}= 0) and stretched (ε_{22}= 0.2) configurations of the stainless steel kirigami patches with different arrangements of spikes including Unidirectional (1Dir), Mirror, Alternating rows, 3-column, and Checker that were considered for this study. Scale bar is 10 mm.

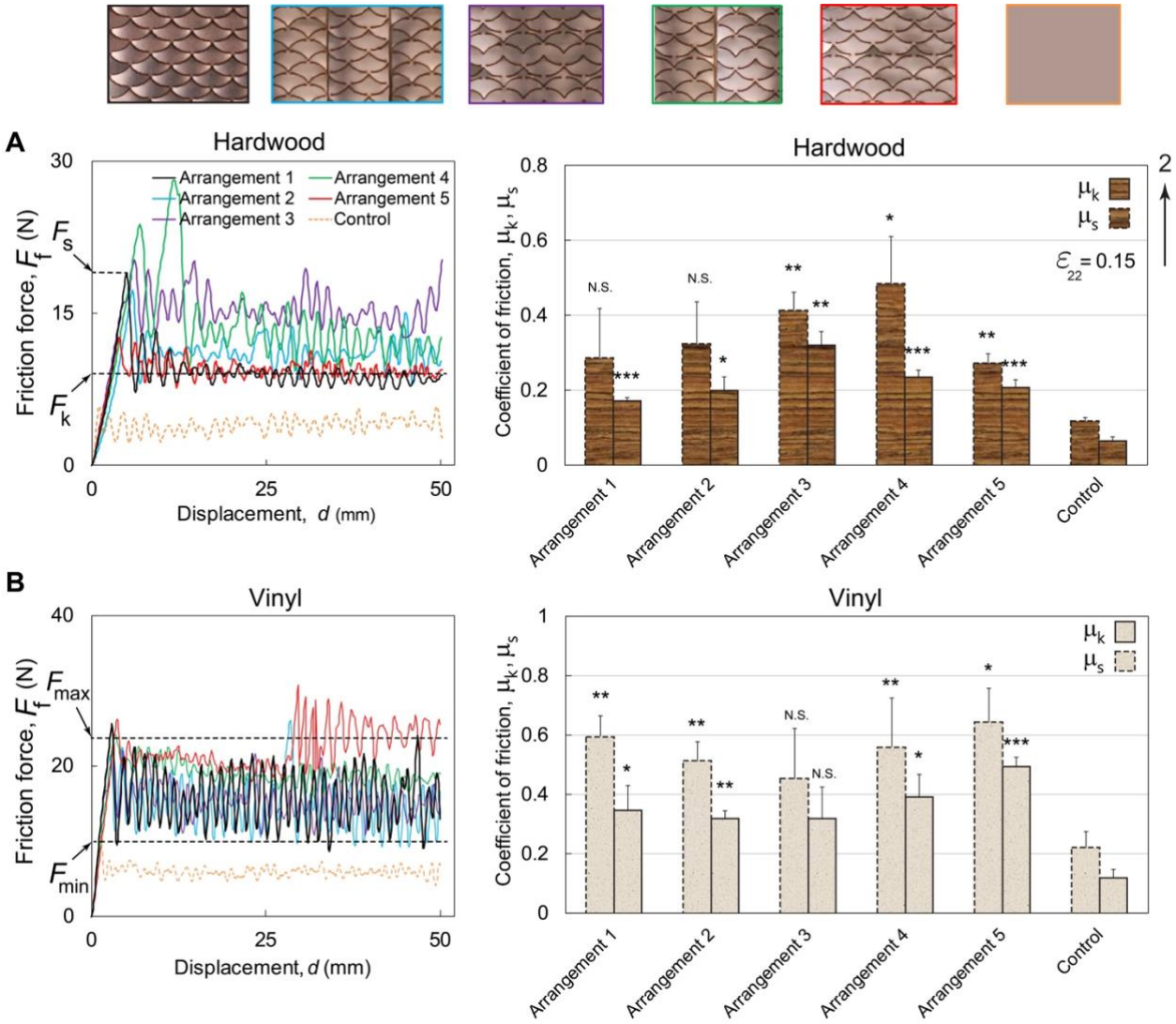

Fig S6. Friction enhancement of the concave kirigami shoe grips with various spike arrangements. Friction force (F_f) vs. displacement (d) response of the concave kirigami surfaces with different spike arrangements prestretched at $\varepsilon_{22} = 0.15$ and control flat surfaces (orange), sliding on (**A**) hardwood, and (**B**) vinyl surfaces. F_s and F_k are the static and kinetic friction forces. Effect of different spike arrangements on static and dynamic friction coefficients (μ_S and μ_K) for kirigami surfaces prestretched at $\varepsilon_{22} = 0.15$ are reported on the right. The different arrangements of the fabricated kirigami grips including arrangement 1 (Unidirectional in black), arrangement 2 (3-column in blue), arrangement 3 (Alternating rows in purple), arrangement 4 (Checker in green), and arrangement 5 (Mirror in red) are shown in the top. Interestingly, all the kirigami demonstrated enhanced frictional properties as compared to the control spikeless patch (orange dashed line), showing the smooth sliding for hardwood and stick-slip response for vinyl. The bar plots show considerable increases in μ_s (two- to three-fold) and μ_k (three- to four-fold) in average for all the arrangements with respect to the controls for both hardwood and vinyl. Data reported as mean ± standard deviation for $n = 3$ measurements for each group. Two-sample t tests were used to

determine the significance. *$P < 0.05$, **$P < 0.01$, ***$P < 0.001$, and N.S. not significant (kirigami patch versus control flat surface for both μ_S and μ_K).

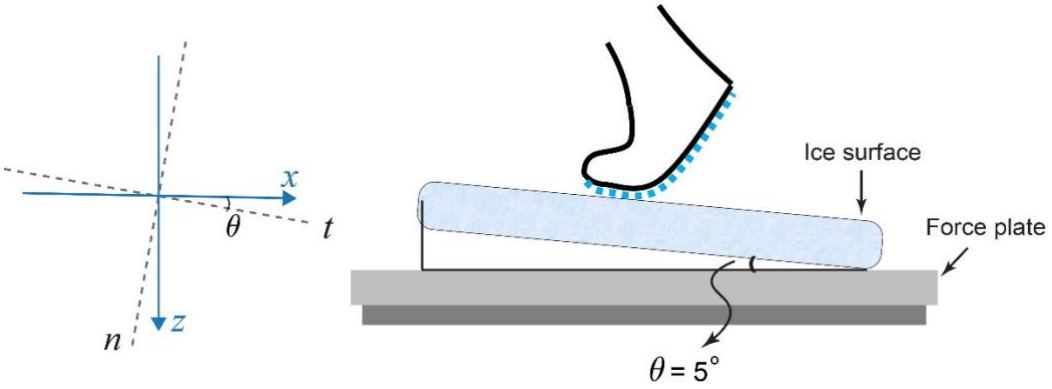

Fig S7. Illustration of force plate testing set-up on an inclined ice surface.

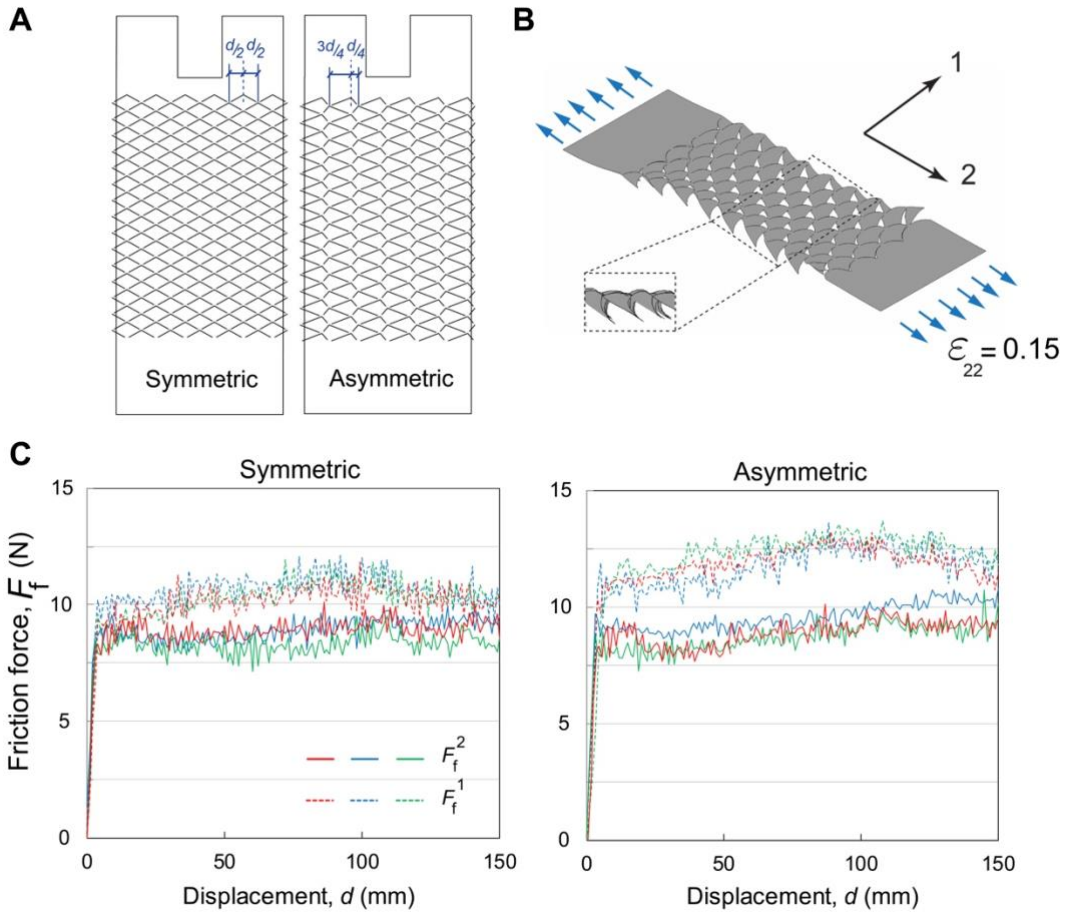

Fig. S8: Biaxial friction control using kirigami surfaces. (**A**) CAD models of triangle kirigami surfaces with symmetric and asymmetric arrays of spikes. d is the width of a unit cell. (**B**) The kirigami can be stretched $\varepsilon_{22} = 0.15$ in 2-direction that results in out of plane buckling of the spikes. (**C**) Friction forces (F_f) between kirigami (prestretched at $\varepsilon_{22} = 0.15$) with symmetric (left plot) and asymmetric (right plot) array of spikes and hardwood surface as a function of displacement. F_f^1 and F_f^2 are the recorded friction forces in 1- and 2-directions, shown by dashed and solid lines, respectively. Each test was performed three times shown by different colors.

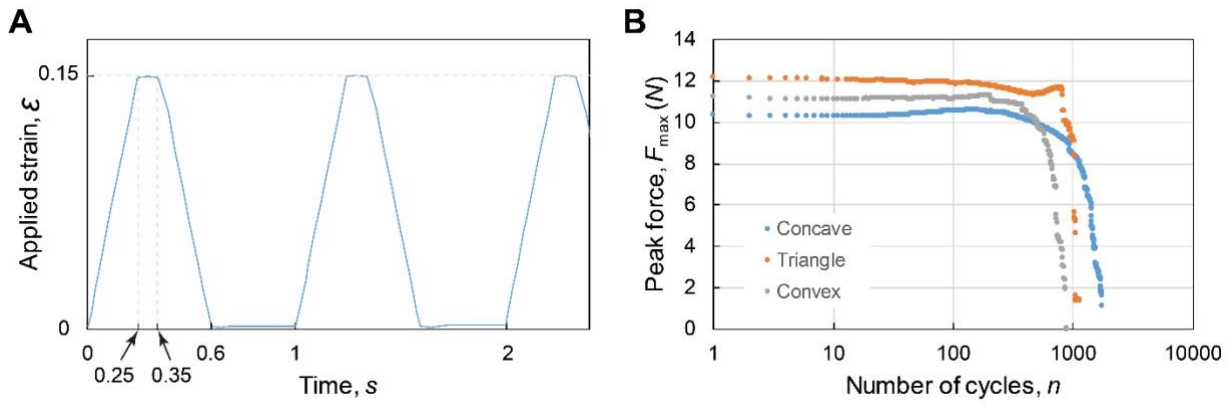

Fig. S9: Experimental fatigue tests. (**A**) Trapezoidal waveform used in the cyclic tests to control the applied strain. (**B**) Maximum recorded applied force, F_{max}, versus the number of loading cycles, n, for the kirigami structures with concave, triangle, and convex spike shapes.

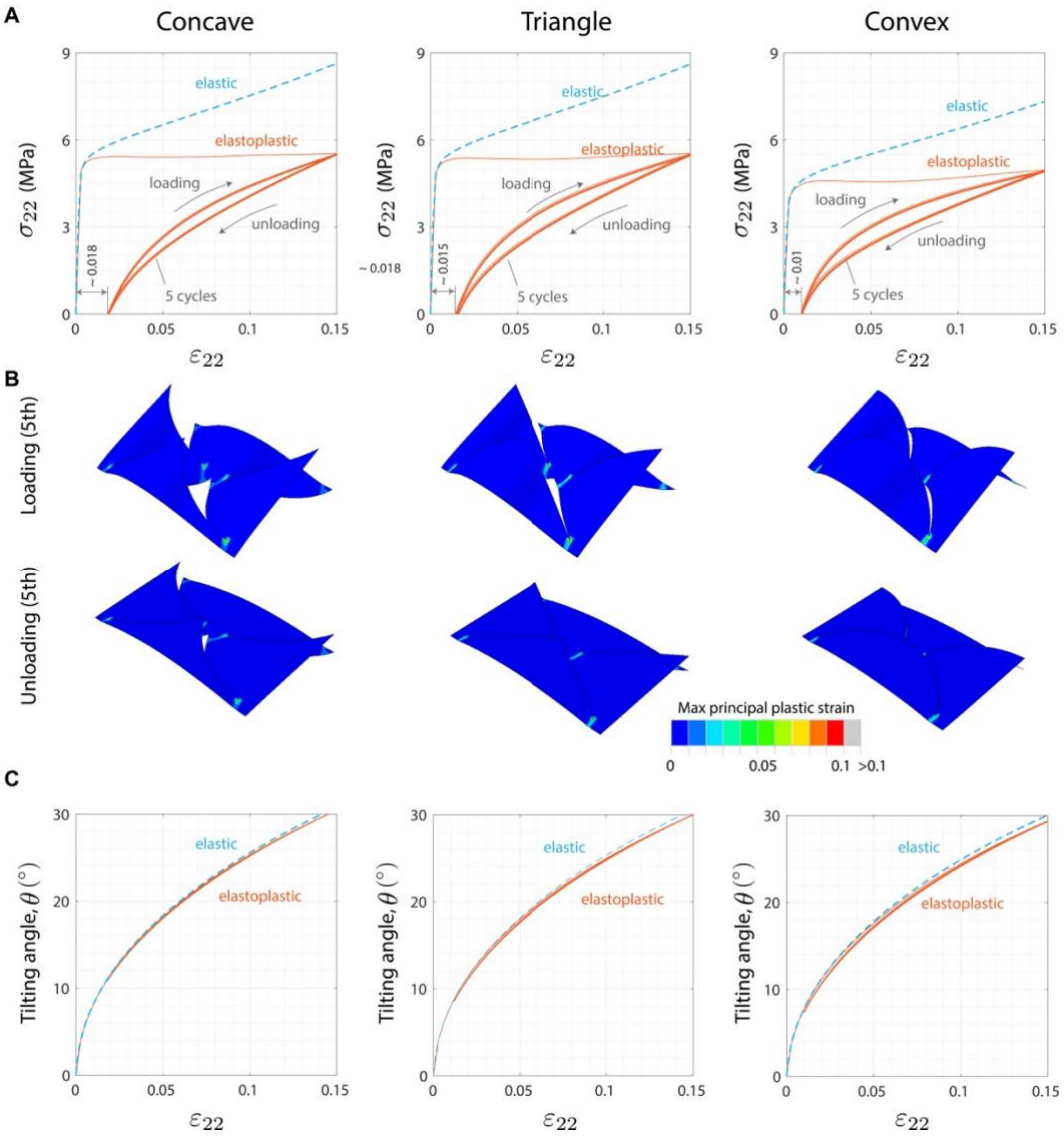

Fig. S10: Effect of material behavior on the response of kirigami structures subjected to uniaxial tension. (**A**) Comparison between numerical stress–strain curves obtained considering a purely elastic (blue dashed lines) and an elastoplastic (orange solid lines for five cyclic loads) material model. Results are reported for concave, triangle, and convex spike shapes steel kirigami patches, characterized by $\gamma = 30^{o}$, $\delta/l = 0.15$ with the residual macroscopic plastic strains 0.018, 0.015, and 0.010, respectively. (**B**) Snapshots showing the distribution of max principal plastic strains at buckled (loading at ε_{22}= 0.15) and released (unloading at ε_{22}= 0) configurations for 5 cyclic uniaxial tensile loads. (**C**) Comparison between the evolution of tilting angle of the spikes (θ) as a function of applied strain (ε_{22}) for a purely elastic (blue dashed lines) and an elastoplastic (orange solid lines for five cyclic loads) material model.

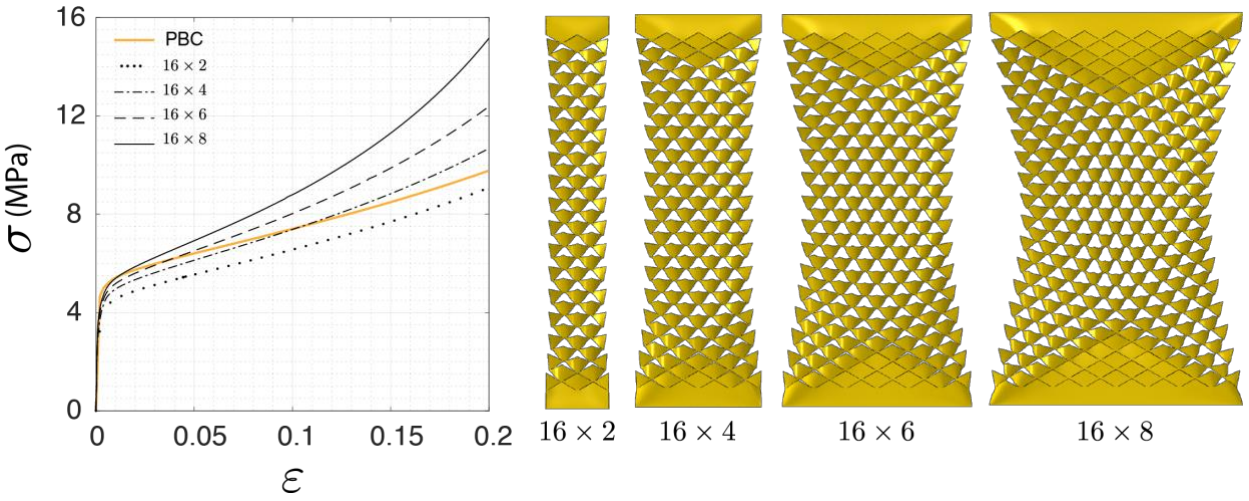

Fig. S11: Stress-strain response of the finite size kirigami under uniaxial tension. Comparison between the response of finite size samples (comprised of 16×2, 16×4, 16×6, 16×8 units) and infinitely large periodic structure (PBC) under uniaxial tension for triangular cut pattern obtained from FEA.

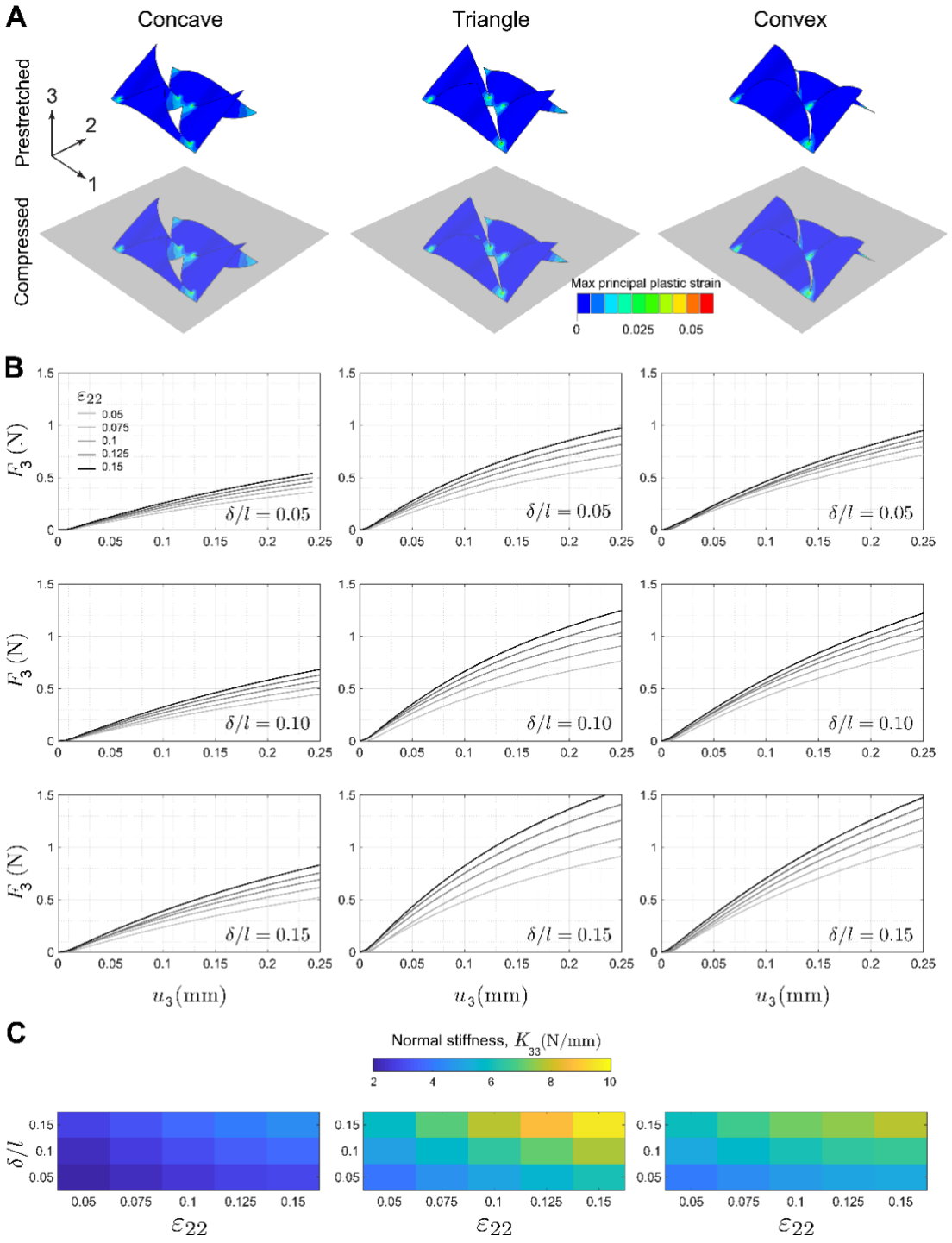

Fig. S12: Evolution of normal stiffness of the kirigami surfaces. (**A**) FEA simulation of periodic kirigami unit cells which are prestretched ($\varepsilon_{22} = 0.15$) and subsequently compressed with a rigid plate. (**B**) Normal force-displacement curves for the different cut patterns and hinge width δ/l under different levels of applied strains ε_{22}. (**C**) Effect of δ/l on the stiffness in 33-direction (K_{33}) of the kirigami spikes with concave, triangle, and convex shapes with γ =30₀ as a function of ε_{22}.

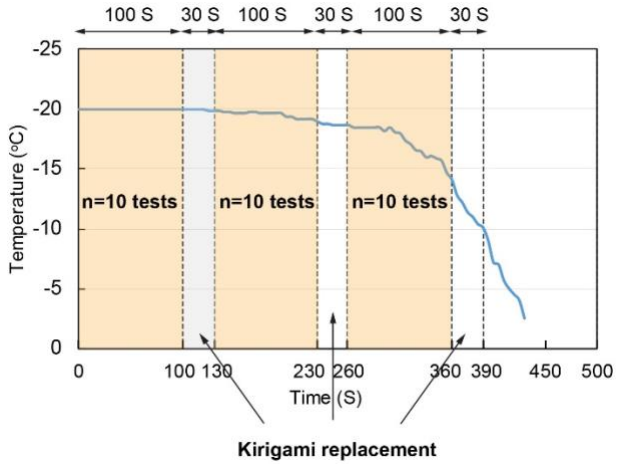

Fig. S13: Variation of ice surface temperature during human force plate measurement of friction with kirigami shoe grips. The temperature of ice blocks during the experiments was monitored using a K-type thermocouple embedded into the top surface. The average of temperature variations recorded over t=7 min for n=30 force-plate human tests (10 measurements per 100 S time periods with 30 S time interval between for replacing the kirigami shoe grips).

Movie S1. Steel kirigami shoe grips attached to a shoe sole. The slip-resistant assistive kirigami metasurface attached to a shoe sole undergoes a shape transformation from a flat surface (corresponding to low friction) to the 3D textured surface with popped-up spikes (corresponding to high friction). This reversible shape transformation caused by bending of the show sole, which induces stretching in the patches, resulting in buckling out the spikes that enables us to tune friction actively and subsequent resistance to slips and falls.

Movie S2. Finite element simulation of kirigami unit cell. A periodic kirigami unit cell with concave spikes is initially stretched up to $\varepsilon_{22} = 0.15$ and then compressed in the normal direction by pushing down a rigid plate against it. The contours in top left panel shows distribution of max principal plastic strain during the deformation. The plastic strains localized in the hinges are moderate and the residual plastic strain is ~ 2%.